Journal of Materials Chemistry A

Accepted Manuscript

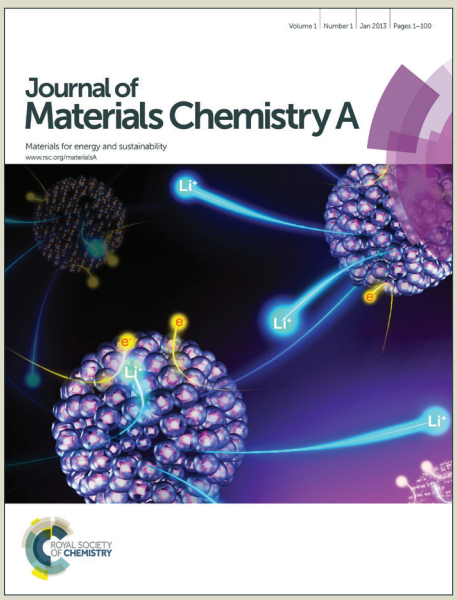

ROYAL SOCIETY OF CHEMISTRY

www.rsc.org/materialsA

Journal of Materials Chemistry RSCPublishing

ARTICLE

Visualizing Order in Dispersions and Solid State Morphology with CryoTEM and Electron Tomography: P3HT:PCBM Organic Solar Cells

Cite this: DOI: 10.1039/x0xx00000x

Received ooth January 2013,
Accepted 00th January 2013

DOI: 10.1039/x0xx00000x

www.rsc.org/

Maarten J. M. Wirix,[a,b] Paul H. H. Bomans,[a] Marco M. R. M. Hendrix,[a] Heiner Friedrich,[a] Nico A. J. M. Sommerdijk[a] and Gijsbertus de With[a,*]

Building blocks for organic solar cells are made from P3HT in a P3HT:PCBM solution in toluene and used to tune the morphology of the photoactive layer. The approach presented here decouples the structure and morphology formation, providing precise control over both the structures in solution and the morphology of the photoactive layer. For the characterization of the nanostructures in the organic casting solutions, cryo-TEM was successfully employed, and reveals the P3HT crystals and even the 1.7 nm lamellar stacking, which in combination with cryogenic low dose electron diffraction clearly proves the high crystallinity of P3HT aggregates realized. The photoactive layers made from pre-crystallized solutions show a morphology that is closely related to the structures in solution. A clear trend of decreasing open circuit voltage and increasing short circuit current with increasing order in the casting solutions and the devices was observed, which correlates with the evolution of the morphology from very intermixed with small fibrillar structures to phase-separated with large polymer crystals, as evaluated from representative devices, characterized in 3D with electron tomography.

Introduction

Organic solar cells are promising as a novel green technology due to their printability, flexibility, light weight and low production cost as major advantages. Their performance depends strongly on the nanoscale morphology of the active layer, which is typically a bulk heterojunction of an electron donor and acceptor phase with ideally an optimized balance between a large interface area for exciton dissociation and phase continuity for charge percolation.[1] Also the crystallinity of the different phases is of importance as charge carrier mobility is directly related to the degree of order in these layers.[2] Ordering in such devices strongly depends on the processing method and further post-processing treatments such as thermal annealing, slow drying or solvent/vapor treatment.[3-5] However, post-processing treatments are cumbersome for the manufacturing process. Annealing is not compatible with the commonly used PET and PEN flexible substrates that have a glass transition temperature of 70 °C and 120 °C, respectively.[6] Solvent annealing and controlled drying methods prevent rapid manufacturing and are hard to control. Therefore post-processing treatments are not suitable for cost-effective large scale production.

The use of regioregular poly-(3-hexylthiophene) (P3HT) as electron donor and (6,6)-phenyl-C61-butyric acid methyl ester (PCBM) as the electron acceptor provides reliable solar cells under a wide variety of processing conditions.[7-10] Although more efficient donor-acceptor combinations have been developed,[11] P3HT is one of the most cost-effective materials for large scale production of organic photovoltaic devices.[12] P3HT can form well-defined highly crystalline nanowires in solution, e.g. through modulation of the solvent quality, temperature or using templated assembly.[13-22] Devices processed from these dispersions display an increased power conversion efficiency as compared to non-prestructured devices, as a consequence of the presence of a highly crystalline, nanostructured network.[23-26] It is therefore of interest to consider growing crystalline nanostructures in solution, to make an ink from the resulting dispersion. Subsequently the ink can be processed to directly create an optimal morphology, thereby decoupling nanostructure formation and device fabrication, so that the latter no longer depends on the deposition process. Achieving control over crystallization may further provide access to new morphologies that would be difficult or impossible to create by post-treatments due to the limited conformational mobility of the polymers in the photoactive layers.

Here, we investigate a P3HT:PCBM system in which we allow the P3HT to crystallize in a casting solution of toluene prior to

the device preparation. Although cryo-TEM of aqueous solutions is well-known, cryo-TEM using organic solvents is a much more difficult technique. To study preformed nanofibers of P3HT in solution, we used toluene, an unconventional solvent in the field of OPV since it generally does not yield the best efficiency devices, but selected, because it is known to form stable vitrified films, an absolute necessity to investigate the structure of P3HT in solution. Typical OPV processing solvents (e.g., ortho-dichlorobenzene) are slowly evaporating and can induce crystallization of the polymer during deposition, making it difficult to determine if crystallization happened in solution or during processing. Moreover, in future solvents like oDCB will be most likely banned.

To investigate the structure and morphology in solution and the resulting devices we use energy filtered (cryo-)TEM and electron tomography – techniques that have shown to be important tools in the analysis of complex organic assemblies[27-33] – in conjunction with low dose electron diffraction and UV-Vis measurements. Through this direct visualization we are able to demonstrate how the morphology and crystallinity of P3HT nanowires and their distribution throughout the P3HT:PCBM photoactive layer affect the open circuit voltage V_{oc} and short circuit current J_{sc} and hence the device performance. In other papers[15,26] the emphasis is on creating optimized devices, which is achieved by adding a significant amount of amorphous P3HT to the mixture, so that the final morphology of the device largely depends on how this dispersion is processed. These papers inspired us to try to elucidate structure formation. Hence the present work does focus on characterization of the structure in solution, the device morphology and performance, exemplified with the P3HT:PCBM model system. This is, to our knowledge, the first time a direct link is made between structure in the casting solution, photoactive layer morphology and device properties, which is made possible by using cryo-TEM employing an organic solvent.

Experimental

Materials

Poly(3-hexylthiophene), P3HT (Plexcore OS2100, M_w = 105000 g mol^{-1} (SEC) and 29200 g mol^{-1} (as determined from the limiting behavior of the low q-part of small angle neutron scattering data of solutions)[34], PDI = 2.1, regioregularity = 99% (NMR) was supplied by Plextronics. (6,6)-Phenyl-C61-butyric acid methyl ester, PCBM (Purity > 99%) was purchased from Solenne BV. The solvent used was toluene (anhydrous, 99.8%) from Sigma-Aldrich. All materials were used as received without further treatment.

Nanostructure fabrication

Crystalline nanowires of P3HT were formed by heating solutions containing 1 wt% of P3HT:PCBM (1:1) in toluene to 70 °C for > 8 hours, subsequently cooling to 38 °C at a rate of 1 °C/min, and keeping the solution at this temperature for 0, 1, 7 and 16 days under constant stirring to prevent sedimentation. This procedure promotes the formation of P3HT nanowires without immediately trapping the polymers in a physical gel.[35] The solutions were immediately used without further purification or re-dispersion in liquid, in order not to alter the composition or structure in the solution. It should be noted that the vapor pressure of toluene is high enough to prevent significant crystallization during processing, such that the structures observed in solution are as close as possible to those in the functional devices (vide infra).

Device fabrication and photovoltaic characterization

Films of P3HT:PCBM were spin-coated from dispersions at 1000-2000 rpm onto cleaned ITO patterned glass substrates covered with a 40 nm thick layer of PEDOT:PSS (Clevios P, VP Al4083). The dispersions were processed at a higher spin coating speed to compensate for the higher viscosity compared to the solutions. A higher spin coating speed decreases the drying time which will prevent further change to the structures during deposition. The samples were then transferred into a physical vapor deposition (PVD) chamber to evaporate 1 nm of LiF and 100 nm of Al in vacuum.

Current-voltage characteristics were measured with a computer-controlled Keithley 2400 source measure unit. Illumination was done by tungsten-halogen lamp filtered by a Schott GG385 UV filter and a Hoya LB120 daylight calibrated at 100 mW cm^{-2}. The thickness of the P3HT:PCBM photoactive layers was determined by a Dektak surface profiler to be 120 ± 10 nm.

UV-vis spectrometry

UV-vis absorption spectra of the solutions were acquired by using A DT-Mini-2GS UV-VIS-IR light source was connected to a Qpod for temperature control and a USB4000 detector, from Ocean Optics with optical fibers. Solutions were diluted 1:10 and injected in a 0.1 mm quartz flow-through cuvette just before spectrum acquisition. The dilution is necessary to measure the absorption peak due to limited transmission in the region where P3HT absorbs the most light. This didn't change the form of the rest of the spectrum and consequently the structures in solution. The absorption spectra of the devices were measured by connecting the light source and detector to a slide holder with optical fibers.

X-ray diffraction (XRD) measurements

The X-ray diffraction patterns of the devices were acquired on a Rigaku Geigerflex Powder Diffractometer, Bragg-Brentano configuration with a secondary graphite monochromator, using Copper (Cu) Kα radiation with wavelength 1.54056 Å at 40 kV and 30 mA. The scans were performed with 2θ from 2-90 degrees with a 0.02 degree step size and a dwell time of 10 s. The diffraction peaks of the aluminum electrodes are used to compensate for the possible peak position shift.

Cryo-TEM characterization

To make a vitrified layer of toluene, a vitrification robot (FEI Vitrobot Mark III) was used. Quantifoil R2\2 200-mesh Cu

grids were purchased from Quantifoil Micro Tools GmbH. 3 µL of solution/dispersion was taken and brought on the Cu grid with a pipet at 38 °C inside the vitrobot chamber. The chamber was saturated with toluene vapor at a temperature of 38 °C to prevent sample evaporation and the accompanied temperature decrease. Subsequently, the grid was blotted for 2 s with filter paper and plunge-frozen in liquid nitrogen. The samples were then kept in liquid nitrogen and loaded into the TU/e Titan Krios (FEI) equipped with a field emission gun operating at 300 kV and the energy slit width was 20 eV centered on 0 eV. Images at low magnification (Figure 1a-c) were recorded at a dose rate, calibrated to 500 $e^- nm^{-2} s^{-1}$, with exposure times of 2 s, using a 2k × 2k Gatan charge-coupled device (CCD) camera. Low dose electron diffraction (LDED) patterns in cryo TEM and convential TEM were acquired at a dose rate of 100 $e^- nm^{-2} s^{-1}$ with exposure times of 5 s. Lower dose rates were observed to do less damage to the crystalline order, yielding higher quality diffraction patterns.

Bilayers and microtome sectioning

Amorphous films of P3HT and PCBM were created by spin coating 1 m% solutions in chloroform on a PEDOT:PSS covered glass substrate. The PEDOT:PSS was subsequently dissolved into water and the films were floated unto a water surface. The films were then picked up by a flexible transparent PET substrate. These films were then sandwiched together to create a bilayer. With microtome sectioning, sections of about 100 nm were created and deposited on Quantifoil R2\2 200-mesh Cu grids.

TEM/ET characterization of the photoactive layers

The P3HT:PCBM layers were floated from water-soluble PEDOT:PSS onto the surface of demineralized water and picked up with Quantifoil R2\2 200-mesh Cu grids. TEM images, electron tomography, and electron diffraction patterns were acquired on the TU/e Titan Krios (FEI) 300 kV operated at room temperature. An energy filter was used to enhance contrast in all acquisitions. The energy slit width was 20 eV centered on 0 eV. The tilt series were acquired in the bright-field mode at a constant defocus of -10 µm in the tilting range from −70° to 70°, by using a linear tilt scheme with an increment of 2° and a dose distribution factor of 1.2. The dose rate was calibrated to 500 $e^- nm^{-2} s^{-1}$, with exposure times of 2 s and a total accumulated dose of 7×10^4 $e^- nm^{-2}$. At this electron flux and dose no structural degradation of the sample was observed during acquisition. The alignment of the tilt series was based on the manual tracking of 10 nm Au fiducial markers. The tomography series were acquired with the Xplore3D software, the alignment and reconstruction was done with IMOD[36] and visualization of the 3D reconstructed volume was done with Avizo 7.1 (Visualization Sciences Group, FEI.) A SIRT (simultaneous iterative reconstruction technique) algorithm with 5 iterations was used for the reconstruction.

Segmentation of the tomogram

Segmentation of the reconstruction of the dispersion device was done meanwhile applying noise reduction using a nonlinear anisotropic diffusion filter.[37] Next a cross-correlation was calculated between the 3D volume and a series of spheres that have a size comparable to the feature size of the nanowires. This way we get a 3D correlation map that preferentially selects the nanowires. Next the wires were segmented out by using a top hat threshold. If the two phases would be completely demixed, we would have 53% P3HT and 47% PCBM, as can be calculated from the densities of 1.15 and 1.3 g cm^{-3} of P3HT and PCBM,[38] respectively, and the 1:1 mass ratio used. Therefore the threshold value was chosen as such that we have 53 vol% P3HT versus and 47 vol% PCBM. All voxels above the threshold are 1, below 0. Subsequently a binary model can be generated like in Figure 4 (left).

Results and discussion

Structure in solution

At 0, 1 and 16 days, the obtained P3HT solutions/dispersions were vitrified and inspected by cryo-TEM to monitor the evolution of the nanostructures (Figure 1a-c). In the initial stages no clear nanostructure formation was visible (Figure 1a), and indeed UV-vis spectra (Figure 1f) indicated a molecularly dispersed solution of the two macromolecules. However, after 1 day the P3HT phase segregates, generating domains of varying density, shown as large scale contrast differences in the images and very small nanofibers nuclei with widths of < 8 nm and lengths of ~100 nm (intermediate state in Figure. 1b). These grow out to form a dispersion of nanowires of ca. 25 nm wide and > 1 µm long (Figure 1c). Liu et al. report nanowires with a width of 7.3-14.4 nm[39] for M_n ranging from 6-33.5 kg mol^{-1} as measured by SEC. Since the P3HT used here has a higher Mn of 50 kg mol^{-1} (SEC), the larger width can be explained by the longer polymer chains. Samitsu et al. report nanowires with a width of 24-27 nm[24] for Mn = 44.9 kg mol^{-1} (SEC). However, the height as reported by Samitsu et al. is only 2-4 nm, which is not comparable to the thick stacks that we observe in cryo-TEM (Figure 1e). It is apparent that with different solvents and processing conditions different P3HT morphologies can be achieved and that the Mw has an effect on the wire morphology. However, since we observed that SEC generally overestimate Mw with a factor of 3-6 for this material, it is hard to compare these data. Brinkmann et al.[40] identified the existence of amorphous interlamellar zones in P3HT thin films grown by directional epitaxial solidification. This indicates that in the 25 nm wide P3HT nanowires amorphous and disordered regions will exist and affect the charge transport through this phase.

The 7, 10 and 16 days samples are all dispersions that showed the same features in the images. These three dispersions are represented here as the 16 days image. This indicates also that the structures in the dispersions are stable for at least a week. High resolution cryo-TEM images of various stages are provided as Supporting Information and indicate a highly anisotropic growth of the nanowires.

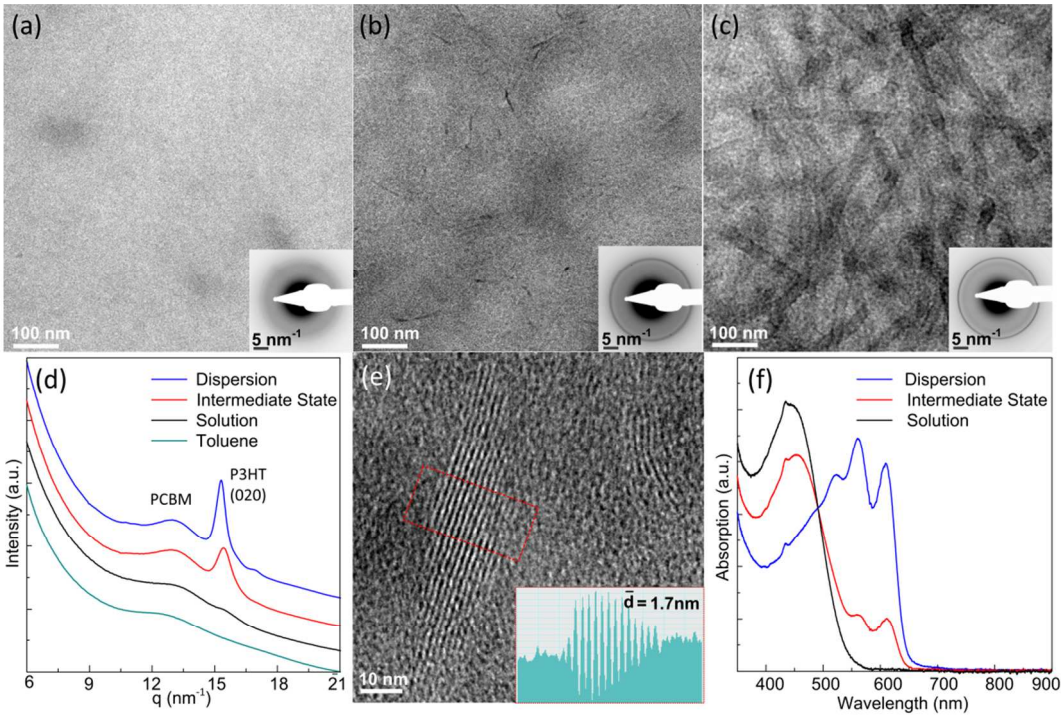

Figure 1: (a-c) CryoTEM images of P3HT:PCBM 1:1, 1 mass% in toluene subsequently vitrified, aged for 0 days (solution), 1 day (intermediate state) and 16 days (dispersion), respectively. The P3HT is dark against a light background of vitrified solvent and PCBM. The insets are the LDED patterns corresponding to the images. (d) Radially integrated LDED patterns. (e) High resolution cryoTEM image of a P3HT nanowire, the inset is the integrated electron intensity profile. (f) UV-vis absorption spectra of the solution/dispersion before vitrification.

Radial integration of the LDED patterns (Figure 1d) revealed that the P3HT developing nanostructures show increasing crystallinity, ultimately displaying a strong (020) reflection associated with the d = 0.39 nm (q = 16.1 nm^{-1}) spacing of the π-π stacking of the thiophene rings. In addition, the final nanowires show two weaker reflections at d = 0.54 nm (q = 11.6 nm^{-1}) and d = 0.35 nm (q = 17.8 nm^{-1}) corresponding to the (300) and (012) planes, respectively. These numbers agree well with the recently reported monoclinic 3D crystal structure of P3HT, derived from X-ray diffraction, with lattice constants a = 1.64 nm, b = 0.76 nm, c = 0.77 nm and γ = 87°.[41,42] In the intermediate state and in the dispersion, an additional diffuse band at d = 0.46 nm (q = 13.6 nm^{-1}) is observed, that has been attributed to densely and homogeneously distributed nanocrystalline PCBM.[43] This indicates that although the crystallinity of P3HT increases dramatically in time, PCBM (diffuse band at d = 0.46 nm) remains in a constant nanocrystalline state. On a timescale of weeks the nanocrystalline PCBM remains stable in solution. We did not observe that PCBM acted as a nucleation site for P3HT, although this can never be completely excluded. However, we did observe that the presence of PCBM slows down the crystallization of P3HT (see Supporting Information)."

The structural organization along the (100) direction was also observed directly from the ~1.7 nm repeat of lamellar stacks in high resolution cryo-TEM images (Figure 1e). The lamella are made from the π-π stacked conjugated backbones of the P3HT. These lamella are held together by the aliphatic interactions between the hexyl side chains of the P3HT. The alternating higher electron density regions of the π-π stacked conjugated backbones and lower electron density regions of the hexyl side chains, which scatter the electrons weaker, shows up as a repeat pattern, which can also be seen from the integrated intensity profile. The HR cryo-TEM images show wires from the side view. A height of the nanowire of 10-20 nm can be estimated from this data.

The crystallization of the nanowires was also observed in the UV-vis absorption spectra (Figure 1f). A single broad peak at λ_{max} = 445 nm is split with evolution of the nanostructures into two maxima at 570 nm and 612 nm. This can be attributed to an increase in conjugation length of the polymer, and an increase in interchain coupling, both resulting from the aggregation of P3HT in solution.[44] Since P3HT can easily form a physical gel the UV-vis spectrum alone does not provide sufficient evidence for the existence of the nanowires in solution. Gels from P3HT casting solutions also have been shown to have some degree of ordering though they do not correspond to the dispersion as we acquired here.[45] In this case cryo-TEM and LDED visualize and provide solid evidence for the growth of P3HT nanowires and the nanocrystalline PCBM in solution.

More details on the crystallization mechanism observed in cryo-TEM can be found in the supporting information (Figure S2)

Photoactive layer morphology

By spin coating the initial solutions, intermediate state solutions and dispersions (aged for different periods) polymer solar cells were prepared with comparable photoactive layer thickness

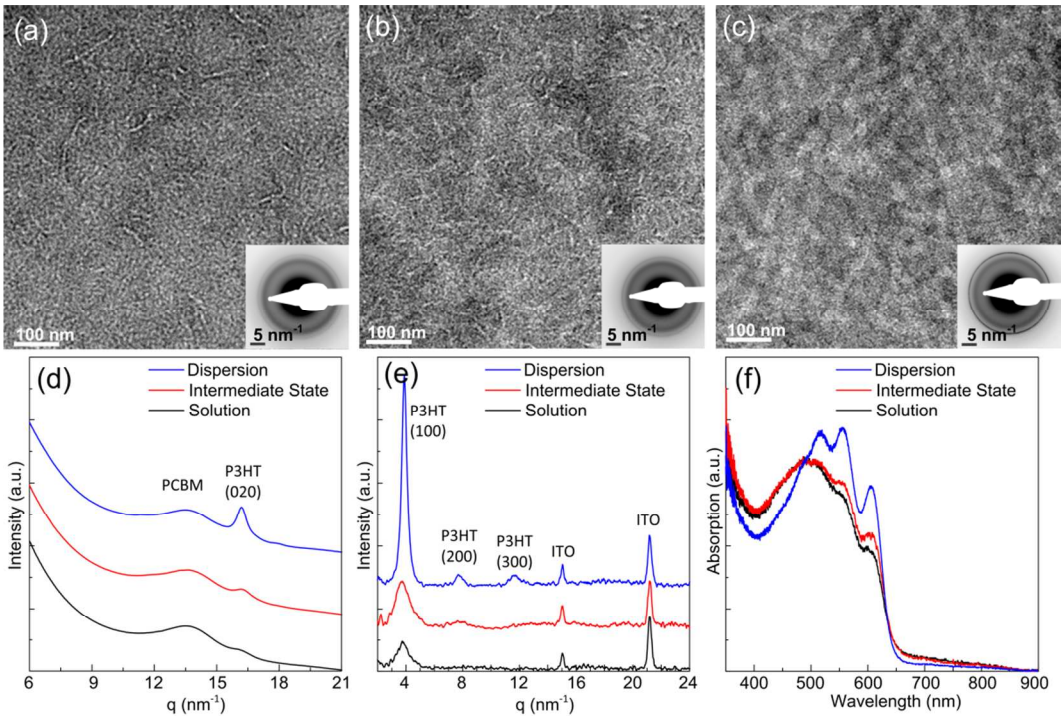

Figure 2: (a-c) TEM images of photoactive layers of the solution, intermediate state and dispersion device, respectively. The P3HT is light and PCBM dark. The insets are the LDED patterns corresponding to the images. (d) Radially integrated LDED patterns. (e) WAX diffraction patterns of the photoactive layers. (f) UV-vis absorption spectra of the photoactive layers. The error bars correspond to a 95% confidence interval. Please note that the final PCBM has a higher density than P3HT, so that the contrast is inverted and P3HT will show up as lighter areas. In contrast the cryoTEM images show P3HT as dark areas against a background of vitrified solution of PCBM in toluene.

(120 ± 10 nm). Our idea is to incorporate the structure in solution directly into the device morphology, for a better understanding of the function of these nanostructures in a functional device. To prevent additional structure formation during processing the drying time during processing was kept as short as possible.

As shown in Figure 2a-c, a structure evolution in the photoactive layers, similar as observed in the solutions. Note that the nanocrystalline PCBM in the photoactive layer is a stronger scatterer than the P3HT, hence the contrast is inversed, compared to the cryo-TEM images. The P3HT is light and the PCBM is dark. In the devices processed from the initial solution (Figure 2a) only small, fiber-like structures of P3HT are visible, which have most likely been formed during processing, since we do not observe them in cryo-TEM. They do not have a preferential orientation and are usually curved. In the photoactive layers processed from the intermediate state dispersions, depicted in Figure 2b, the same phase segregation is observed as in solution. This is manifested as lighter regions, which are P3HT-rich and darker regions, which are PCBM-rich. In addition white thin P3HT fibers can be abundantly seen similar to the nuclei, observed in cryo-TEM. These fibers are not significantly different from the ones in Figure 2a, although they originated from the processing and the ones in Figure 2b from nucleation in solution and partly from processing. The devices prepared from the aged dispersions showed the same nanowires of ca. 25 nm wide and > 1 µm long as we observe in the cryo-TEM images (Figure 2c). In contrast with the former fiber-like structures, these nanowires are rigid and their lamella lie consistently parallel to the substrate, which can be deducted from the constant 25 nm width of the nanowires as well as from the absence of the (100) reflections in the LDED patterns. Because most of the polymer phase is incorporated in the nanowires, there is no significant change in structure during processing.

The radially averaged LDED pattern in Figure 2d demonstrated, that aging of the solutions leads to an increased crystallinity of the P3HT in the corresponding devices as the P3HT-peak at d = 0.39 nm (q = 16.1 nm^{-1}) becomes sharp and high as compared to the PCBM-peak at d = 0.46 nm (q = 13.6 nm^{-1}). The same state of PCBM is observed in all the photoactive layers. Because the LDED pattern in Figure 1d of the solution did not show the same nanocrystalline PCBM peak, the nanocrystalline PCBM in this case must have grown fast during the deposition process. Comparing Figure 1d and 2d, nanocrystalline, PCBM can grow either during processing or in solution and significantly faster than the P3HT.

The increased crystallinity of P3HT was confirmed by the appearance of a strong (100) reflection at d = 1.7 nm (q = 3.7 nm^{-1}) and the higher order reflections in the wide angle X-ray (WAX) diffractograms (Figure 2e) of the films, as well as by the UV-vis absorption spectrum of the photoactive layers which showed an increasing red shift with increasing aging time of the used solutions (Figure 2f).

With respect to the most stable form of P3HT, Prosa et al.[46] stated in 1996 that it is not clear which form, I (non-

interdigitized side chains) or II (interdigitized side chains), is the most stable one. Rahimi et al.[47] mention that phase II P3HT is the most stable. However, several papers report that phase I P3HT is the most common one.[47,48] Upon heating, form II irreversibly transforms into form I.[48,49] Finally, Poeling et al.[49] provide evidence that phase I is the thermodynamically stable form. This seems to indicate that, even if side chain melting were to happen, phase I P3HT, which we observe here, is the most stable form.

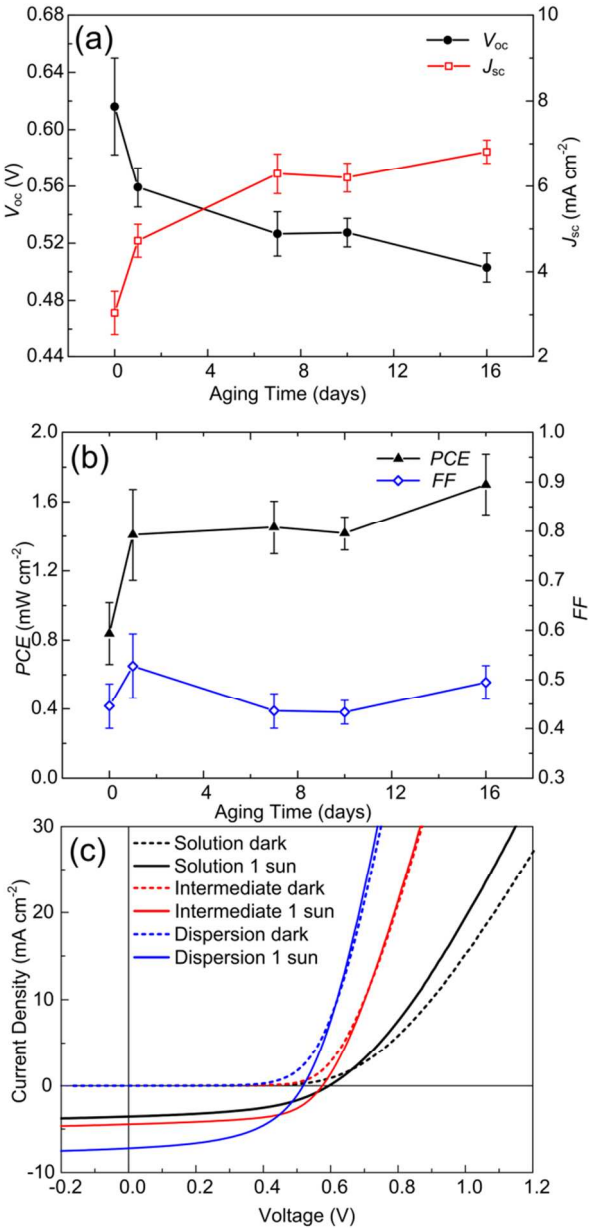

Figure 3: a) Average V_{oc} and J_{sc}. b) PCE and FF of devices at different points in time. c) Typical *JV*-Curves dark (dashed line) and under 1 sun (solid line) for the three different morphologies presented.

It is clear that these structures formed in solution had a large impact on the morphology of the photoactive layers. Our visual data proves that if nanostructures from a pre-crystallized dispersion are fully developed, tuning of the morphology of devices, independent of the way they are processed and without having to use post-treatments, is possible.

Device performance

The average photovoltaic performance of > 12 of these devices was analyzed and the device statistics are shown in Figure 3 and Table 1. Most notably, by increasing the aging time from 0 to 16 days, the short circuit current (J_{sc}) increased by a factor of more than 2, from 3.0 ± 0.4 to 6.8 ± 0.3 mA cm^{-2}. This increase indicates that the device processed from the aged, pre-crystallized dispersion provides more efficient pathways to extract the charges as compared to the device processed from the initial solution.

However, during the crystallization process the open circuit voltage V_{oc} decreased from 0.62 ± 0.03 to 0.51 ± 0.01 V due to a lowering of the P3HT band gap. This is completely consistent with the observation that the energy of the charge transfer state can be significantly lowered for blends with a high crystalline P3HT wire content.[50] The fill factor FF did not show significant improvements giving average values ranging from 0.43 to 0.52. Normally for annealed solar cells, better charge transport properties, due to more phase separation and crystallinity, lead to better fill factors. As a test we annealed some solution cells at 120 °C for 10 min and dispersion cells at 80 °C and we observe an improvement of the FF and the J_{sc}. When annealing the dispersion device at 120 °C, the performance drops dramatically, most likely because the crystallinity is lost and the phase separation becomes too coarse. For the present non-annealed devices, shunts and charge traps are probably the cause for the relatively low fill factors.[51]

Table 1: Device statistics collected as a function of crystallization time in solution. The notation a ± b corresponds to the average value and the 95% confidence interval.

Aging (days)	V_{oc} (V)	J_{sc} (mA/cm^{-2})	FF	PCE (%)	# devices
0	0.62 ± 0.03	3.0 ± 0.4	0.45 ± 0.05	0.8 ± 0.3	32
0 annealed (120 °C, 10′)	0.54 ± 0.02	6.7 ± 0.6	0.56 ± 0.05	2.0 ± 0.5	16
1	0.56 ± 0.01	4.7 ± 0.4	0.52 ± 0.06	1.4 ± 0.3	12
7	0.53 ± 0.02	6.3 ± 0.5	0.43 ± 0.04	1.5 ± 0.2	23
10	0.53 ± 0.01	6.2 ± 0.3	0.43 ± 0.02	1.4 ± 0.1	19
16	0.50 ± 0.01	6.8 ± 0.3	0.49 ± 0.03	1.7 ± 0.2	24
16 annealed (80 °C, 10′)	0.49 ± 0.01	6.9 ± 0.2	0.53 ± 0.01	1.9 ± 0.1	8

The three contributions combined lead to a net gain in performance of 100 % from 0.8 to 1.7 % power conversion efficiency (PCE).

By blending in additional amorphous polymer and using a combination of structure and morphology formation during processing, and using other casting solvents very promising

higher efficiencies (> 3 %) can be achieved.[23,24] However, our aim here was to transfer the structure in the solution in a reproducible way to the device, to understand the function of the nanostructures, which were observed in solution, and to realize an ink containing building blocks for the morphology, rather than realizing optimized devices. The significant trend in V_{oc} and J_{sc} is a consequence of the change in the structures in the dispersions and eventually in the photoactive layer morphologies.

The increase in photocurrent in the devices, the formation of a crystalline network and the decrease of the series resistance of the devices, as can be deduced from the *JV* curves in the first quadrant, are proof that the conductivity increases. The increased conductivity of crystalline P3HT is indicated in several papers, see, e.g., references.[52,53]

Percolating network

To establish a connection between the morphology and the device performance it is important to understand the origin of the contrast between P3HT and PCBM. To provide experimental proof for the existence of contrast between amorphous P3HT and PCBM, a model system was made by microtoming a bilayer of P3HT and PCBM yielding a layer of P3HT and PCBM side-by-side of ~100 nm. These layers were imaged with BFTEM at underfocus values of 0, 5, 10, 15 µm as shown in Figure 4. In regions close to each other but in the different phases, indicated by yellow boxes, intensities are collected and depicted in the histograms next to the micrographs. The histogram for the 0 µm defocus image clearly shows separated distributions for amorphous P3HT and PCBM indicating amplitude contrast. This originates from the density difference between these two materials. Using larger underfocus values, the P3HT phase becomes more grainy in the image and the intensity distribution of P3HT overlaps more with the one of PCBM. At 10 µm underfocus there is some overlap, but still a significant difference exists between the two distributions. Increasing the underfocus value will also increase the contrast between the crystalline P3HT nanowires and the amorphous structure. By measuring at intermediate defocus values, sufficient contrast between the PCBM and (amorphous) P3HT phase can be obtained. This, in combination with electron tomography on devices, provides valuable information on the morphology.

Another option is to use energy filtered TEM to enhance the contrast between P3HT and PCBM as reported here.[33,54]

To explain the device performance increase in more detail, electron tomography (ET) was performed on three representative devices prepared from a fresh solution (0 days), an intermediate state (1 day) and a final dispersion (16 days). From the 3D reconstructions the phase separation in the three devices becomes clearly visible after segmentation (Figure 5 left). Orthoslices through the reconstructions of the photoactive layers were taken near the Al/LiF electrode, the middle of the device, and near the PEDOT:PSS interface (Figure 5 right). All three reconstructions show a homogeneous distribution of nanostructures of P3HT along the z-height direction. Because we used a fast evaporating solvent and spin coating, the nanostructures did not reorder or interdiffuse, but just spread homogeneously during the drying of the film. It was reported in some instances, that a P3HT:PCBM gradient was present in the photoactive layer of annealed devices.[31] This could imply that

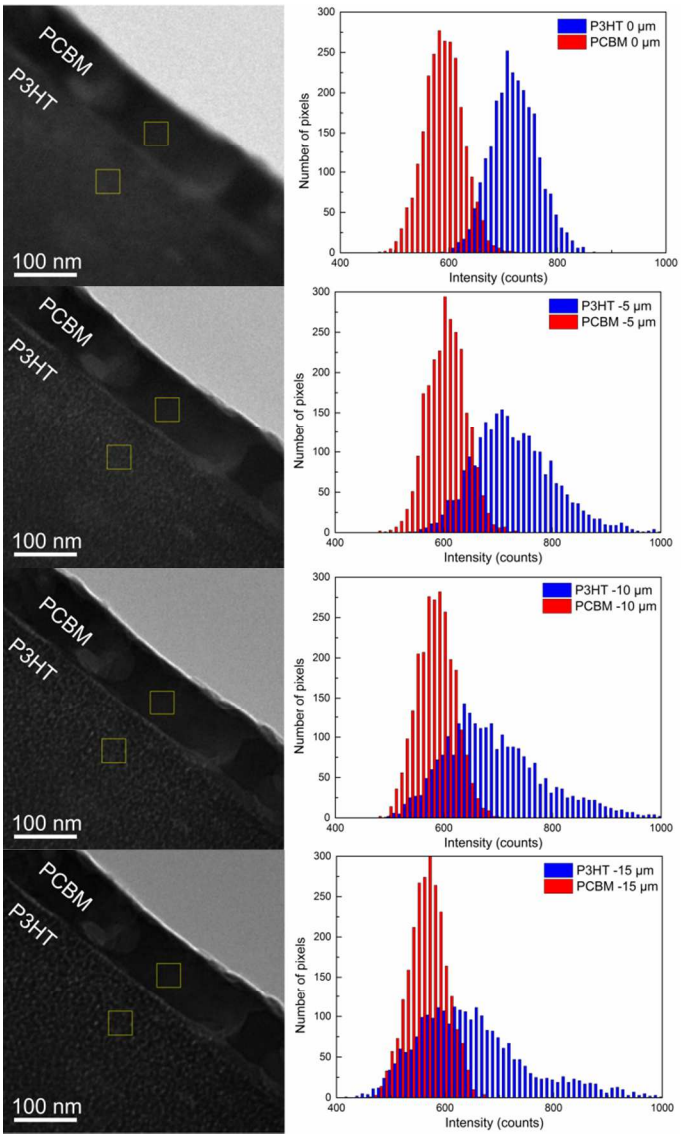

Figure 4: (left) TEM image of a microtomed section of an amorphous P3HT:PCBM bilayer at different defocus values. Defocus equals 0, 5, 10, 15 µm from top to bottom (right) Histograms corresponding to the intensities acquired from the yellow integration boxes on the left. Each integration box spans an area of 2500 pixels. The larger the defocus value the more the intensity distributions overlap.

before annealing there is enrichment of PCBM at the cathode. However, our electron tomograms do not show any form of material gradient and the JV-curves (Figure 3c) do not show an S-shape which is typical for the presence of a blocking layer.[43] In line with the projection images in Figure 2 we observe fine fiber-like P3HT structures throughout the device prepared from the fresh solution. In the device prepared from the intermediate state dispersion these structures become more abundant and slightly wider, while in the device prepared from the aged dispersion the crystalline nanowires have developed even

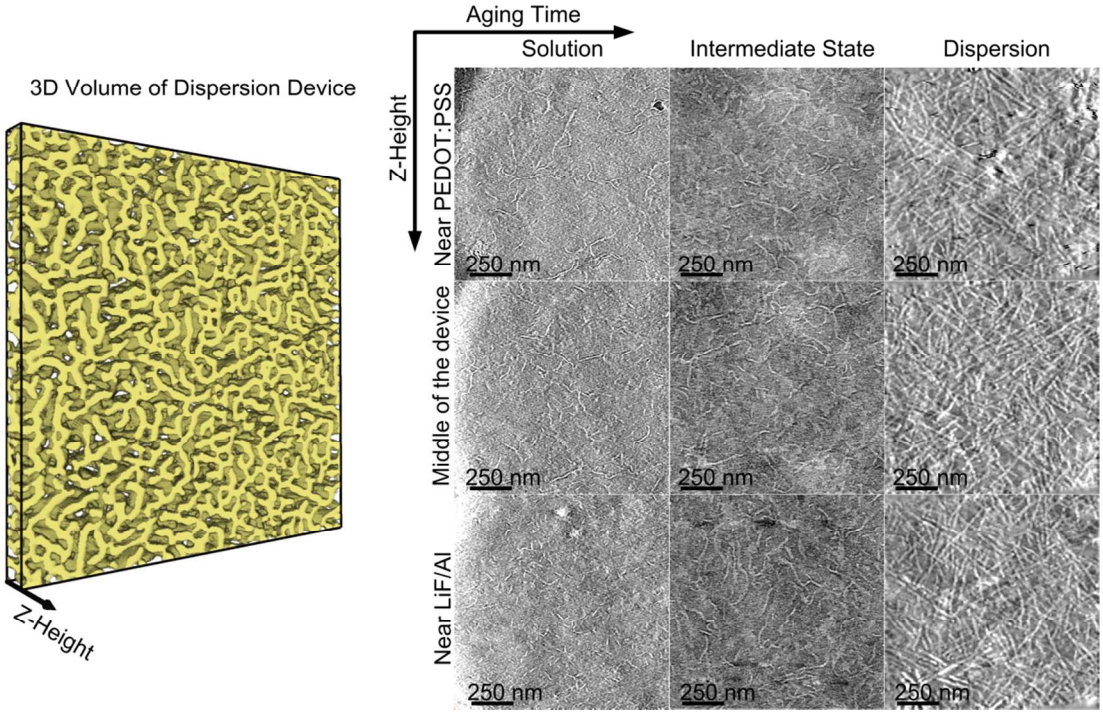

Figure 5: (left) A 3D model of the dispersion device. Inside the black box the yellow phase is P3HT while the transparent phase is PCBM. (right) Slices from the tomographic reconstruction at different locations in the devices.

further and P3HT and PCBM are more phase separated.

The increase in current density must be related to the presence of the broad nanowires which form larger and more phase separated domains in the percolating network throughout the volume of photoactive layer. These larger domains have been reported to significantly reduce the recombination of charges and so improving the charge transport.[55] Further, the crystalline nature of the nanowires and the formation of a crystalline network are also beneficial for the charge percolation,[42] i.e. better hole transporting through the P3HT phase. Moreover, it has recently been shown that the resistance of the bridging points between two wires is significantly lower than the bulk resistance of a single wire,[52] which means that the connection between two wires is not a bottleneck for charge transport. Consequently a close-packed web of wires with this particular morphology increases the current density with increasing aging time of the casting solution. In summary the phase separation introduced by the crystalline network is beneficial for the device performance.

The above conclusion is based on the trend presented in this study. Normally solar cells are made by using slow evaporating solvents and applying annealing to induce phase separation or using new high-performance absorbers with markedly less diffraction strength than P3HT, resulting in much better performing devices. However, when comparing these dispersion born solar cells to the much better performing conventional solar cells, made by deposition and annealing, the general applicability of the above conclusion needs some elaboration. The presence of the crystalline nanowires has an effect on the morphology and the crystallinity. The morphology improvement – clearly visualized in this study – has a much greater impact than the crystallinity. The crystallinity is mildly beneficial because it increases the hole mobility, but on the other hand also significantly decreases V_{oc}. Crystalline nanowires are beneficial because the phase separation they induce, but in many cases more amorphous morphologies have also good percolating properties.[56] However, the idea of a fast deposition of morphology created in a non-halogenated organic solvent has the possibility of decreasing the cost of printing organic solar cells without having to use cumbersome post-treatments or drying in a controlled atmosphere. In this respect the procedure could be useful for more cost-effective production of organic solar cells.

In addition, as the exciton diffusion length (the average distance excitons can diffuse through a phase before recombining) in P3HT is around 8.5 nm,[57] the domain size of the crystalline network ~25 nm is narrow enough to allow most excitons to reach the interface before recombination and at the same time wide enough to sweep out the formed charges efficiently. The 25 nm phase separation has slightly larger dimensions than the 10 nm phase separation that exciton diffusion needs. The latter number, however, is not a hard figure but rather a balance between good charge transport properties and limited exciton recombination losses. Hence, although recombination losses are increased, the improved current seems to dominate the greatly improved charge transport properties. It would be interesting to see what the perfect balance between exciton diffusion and charge transport is, how crystallinity affects exciton diffusion and which role delocalization of the electron wavefunctions play. These points

still need to be investigated.

The connectivity of the phases in the z-height direction is most strongly related to the charge percolation. Often this is extrapolated from TEM projection images or AFM surface plots, but in our case 3D information is provided to clearly show the bulk morphology of the photoactive layer. The reconstructions reveal the nanostructures more clearly compared to the TEM projection image or AFM surface plots, they are homogeneously distributed and form a percolating network and provide an opportunity to do more quantitative analysis to understand how device performance and morphology are related in functional devices.

Conclusions

We have allowed a solution of P3HT:PCBM in toluene to crystallize prior to organic solar cell production. This process was studied for the first time with cryo-TEM — not commonly used for organic solvents — in combination with LDED. Our unique analysis using 2D and 3D TEM and cryo-TEM shows that nanowires with increasing crystallinity form upon aging and that these structures can be preserved during processing. We clearly show that apart from the contrast of the nanowires, there is amplitude contrast between amorphous P3HT and PCBM, which supports our claims about the morphology. The nanostructures were homogeneously distributed throughout the devices. We provided clear evidence for the decoupling of the structure and morphology formation, e.g. no significant additional structure formation happens during processing. Intrinsic to the crystalline structures, there is a small decrease in open circuit voltage. In contrast, the evolution in morphology from very intermixed with a few fibrillar structures to a phase-separated network with large polymer crystals leads to a significant increase in photocurrent.

Understanding the role of morphological variations will be key to the efficient large scale production of polymer solar cells and also opens the road to create more innovative designs for the internal structure of such devices. We demonstrate here that following the structure formation from the solution to the device provides valuable structural information of the materials in solution and in the devices, furthermore this structural study provides valuable information for the application of printing technology for organic solar cells. As the wires studied here seem to be the most stable form of P3HT, their application as preformed structures will prevent significant morphological changes that could affect the long-time performance of many device structures.

Previous cryogenic electron microscopy studies[58,59] have revealed already some insight in photo-voltaic structures. In this paper, the relation between starting dispersions and the resulting photo-voltaic structures is elucidated as an example of how cryo-electron tomography can help to understand the connection between structures in solution and the resulting solid state morphology.

Acknowledgements

A. Hassan is acknowledged for his help with device processing, M. Spapens and L. Mouton for their help with the 3D analysis and A. Spoelstra for the microtoming. We also thank R.A.J. Janssen for the fruitful discussions. This work forms part of the research program of the Dutch Polymer Institute (DPI), Project No. 682. Structure creation in solution.

Notes and references

[a] Soft Matter CryoTEM Research Unit, Laboratory for Materials and Interface Chemistry, Eindhoven University of Technology, P.O. Box 513, Eindhoven, 5600 MB, The Netherlands.

[b] Dutch Polymer Institute (DPI), P.O. Box 902, 5600 AX Eindhoven, the Netherlands.

Electronic Supplementary Information (ESI) available: 3D animation movie of the morphology of a crystalline solar cell device. See DOI: 10.1039/b000000x/

1. G. Yu, J. Gao, J. C. Hummelen, F. Wudl and A. J. Heeger, *Science*, 1995, **270**, 1789-1791.
2. X. N. Yang, J. Loos, S. C. Veenstra, W. J. H. Verhees, M. M. Wienk, J. M. Kroon, M. A. J. Michels and R. A. J. Janssen, *Nano Lett.*, 2005, **5**, 579-583.
3. K. W. Chou, B. Yan, R. Li, E. Q. Li, K. Zhao, D. H. Anjum, S. Alvarez, R. Gassaway, A. Biocca, S. T. Thoroddsen, A. Hexemer and A. Amassian, *Adv. Mater.*, 2013, **25**, 1923-1929.
4. Y. Kim, S. Cook, S. M. Tuladhar, S. A. Choulis, J. Nelson, J. R. Durrant, D. D. C. Bradley, M. Giles, I. McCulloch, C.-S. Ha and M. Ree, *Nat. Mater.*, 2006, **5**, 197-203.
5. H. Li, H. W. Tang, L. G. Li, W. T. Xu, X. L. Zhao and X. N. Yang, *J. Mater. Chem.*, 2011, **21**, 6563-6568.
6. D. Chen and H. G. Zachmann, *Polymer*, 1991, **32**, 1612-1621.
7. M. T. Dang, L. Hirsch and G. Wantz, *Adv. Mater.*, 2011, **23**, 3597-3602.
8. G. Li, V. Shrotriya, J. S. Huang, Y. Yao, T. Moriarty, K. Emery and Y. Yang, *Nat. Mater.*, 2005, **4**, 864-868.
9. W. L. Ma, C. Y. Yang, X. Gong, K. Lee and A. J. Heeger, *Adv. Funct. Mater.*, 2005, **15**, 1617-1622.
10. H. Sirringhaus, *Science*, 1998, **280**, 1741-1744.
11. M. A. Green, K. Emery, Y. Hishikawa, W. Warta and E. D. Dunlop, *Progress in Photovoltaics*, 2013, **21**, 827-837.
12. F. C. Krebs, Espinosa, N., Hösel, M., Søndergaard, R. R. and Jørgensen, M., *Adv. Mater.*, 2014, **26**, 29-39.
13. D. Huesmann, P. M. DiCarmine and D. S. Seferos, *J. Mater. Chem.*, 2011, **21**, 408-413.
14. L. Li, G. Lu and X. Yang, *J. Mater. Chem.*, 2008, **18**, 1984-1990.
15. W. D. Oosterbaan, V. Vrindts, S. Berson, S. Guillerez, O. Douheret, B. Ruttens, J. D'Haen, P. Adriaensens, J. Manca, L. Lutsen and D. Vanderzande, *J. Mater. Chem.*, 2009, **19**, 5424-5435.
16. J. D. Roehling, I. Arslan and A. J. Moulé, *J. Mater. Chem.*, 2012, **22**, 2498-2506.
17. S. D. D. V. Rughooputh, S. Hotta, A. J. Heeger and F. Wudl, *J. Polym. Sci., Part B: Polym. Phys.*, 1987, **25**, 1071-1078.

18. C. A. Sandstedt, R. D. Rieke and C. J. Eckhardt, *Chem. Mater.*, 1995, **7**, 1057-1059.
19. S. Sun, T. Salim, L. H. Wong, Y. L. Foo, F. Boey and Y. M. Lam, *J. Mater. Chem.*, 2011, **21**, 377-386.
20. T. Yamamoto, D. Komarudin, M. Arai, B. L. Lee, H. Suganuma, N. Asakawa, Y. Inoue, K. Kubota, S. Sasaki, T. Fukuda and H. Matsuda, *J. Am. Chem. Soc.*, 1998, **120**, 2047-2058.
21. M. Brinkmann, *J. Polym. Sci., Part B: Polym. Phys.*, 2011, **49**, 1218-1233.
22. M. Brinkmann, F. Chandezon, R. B. Pansu and C. Julien-Rabant, *Adv. Funct. Mater.*, 2009, **19**, 2759-2766.
23. A. J. Moule and K. Meerholz, *Adv. Funct. Mater.*, 2009, **19**, 3028-3036.
24. S. Samitsu, T. Shimomura, S. Heike, T. Hashizume and K. Ito, *Macromol.*, 2008, **41**, 8000-8010.
25. S. Bertho, W. D. Oosterbaan, V. Vrindts, J. D'Haen, T. J. Cleij, L. Lutsen, J. Manca and D. Vanderzande, *Org. Electron.*, 2009, **10**, 1248-1251.
26. S. Berson, R. De Bettignies, S. Bailly and S. Guillerez, *Adv. Funct. Mater.*, 2007, **17**, 1377-1384.
27. H. Azimi, D. Fournier, M. Wirix, E. Dobrocka, T. Ameri, F. Machui, S. Rodman, G. Dennler, M. C. Scharber, K. Hingerl, J. Loos, C. J. Brabec and M. Morana, *Org. Electron.*, 2012, **13**, 1315-1321.
28. H. Friedrich, P. M. Frederik, G. de With and N. A. Sommerdijk, *Angew. Chem., Int. Ed. Engl.*, 2010, **49**, 7850-7858.
29. A. A. Herzing, L. J. Richter and I. M. Anderson, *J. Phys. Chem. C*, 2010, **114**, 17501-17508.
30. S. D. Oosterhout, M. M. Wienk, S. S. van Bavel, R. Thiedmann, L. J. A. Koster, J. Gilot, J. Loos, V. Schmidt and R. A. J. Janssen, *Nat. Mater.*, 2009, **8**, 818-824.
31. S. van Bavel, E. Sourty, G. de With, S. Veenstra and J. Loos, *J. Mater. Chem.*, 2009, **19**, 5388-5393.
32. J. van Herrikhuyzen, S. J. George, M. R. J. Vos, N. A. J. M. Sommerdijk, A. Ajayaghosh, S. C. J. Meskers and A. P. H. J. Schenning, *Angew. Chem., Int. Ed.*, 2007, **46**, 1825-1828.
33. L. F. Drummy, R. J. Davis, D. L. Moore, M. Durstock, R. A. Vaia and J. W. P. Hsu, *Chem. Mater.*, 2011, **23**, 907-912.
34. I. Monnaie, F. Meersman, D. Haynes, R. Schweins, G. de With and E. Nies, *To be published*.
35. G. M. Newbloom, K. M. Weigandt and D. C. Pozzo, *Macromol.*, 2012, **45**, 3452-3462.
36. J. R. Kremer, D. N. Mastronarde and J. R. McIntosh, *J. Struct. Biol.*, 1996, **116**, 71-76.
37. A. S. Frangakis and R. Hegerl, *J. Struct. Biol.*, 2001, **135**, 239-250.
38. J. W. Kiel, B. J. Kirby, C. F. Majkrzak, B. B. Maranville and M. E. Mackay, *Soft Matter*, 2010, **6**, 641-646.
39. J. H. Liu, M. Arif, J. H. Zou, S. I. Khondaker and L. Zhai, *Macromol.*, 2009, **42**, 9390-9393.
40. M. Brinkmann and P. Rannou, *Macromol.*, 2009, **42**, 1125-1130.
41. D. Dudenko, A. Kiersnowski, J. Shu, W. Pisula, D. Sebastiani, H. W. Spiess and M. R. Hansen, *Angew. Chem., Int. Ed. Engl.*, 2012, **51**, 11068-11072.
42. N. Kayunkid, S. Uttiya and M. Brinkmann, *Macromol.*, 2010, **43**, 4961-4967.
43. X. N. Yang, J. K. J. van Duren, M. T. Rispens, J. C. Hummelen, R. A. J. Janssen, M. A. J. Michels and J. Loos, *Adv. Mater.*, 2004, **16**, 802-806.
44. H. Yamagata and F. C. Spano, *J. Chem. Phys.*, 2012, **136**, 184901.
45. Y. Huang, H. Cheng and C. C. Han, *Macromol.*, 2010, **43**, 10031-10037.
46. T. J. Prosa, M. J. Winokur and R. D. McCullough, *Macromol.*, 1996, **29**, 3654-3656.
47. K. Rahimi, I. Botiz, N. Stingelin, N. Kayunkid, M. Sommer, F. P. V. Koch, H. Nguyen, O. Coulembier, P. Dubois, M. Brinkmann and G. Reiter, *Angew. Chem., Int. Ed.*, 2012, **51**, 11131-11135.
48. Y. Yuan, J. M. Zhang, J. Q. Sun, J. Hu, T. P. Zhang and Y. X. Duan, *Macromol.*, 2011, **44**, 9341-9350.
49. C. Poelking and D. Andrienko, *Macromol.*, 2013, **46**, 8941-8956.
50. K. Vandewal, W. D. Oosterbaan, S. Bertho, V. Vrindts, A. Gadisa, L. Lutsen, D. Vanderzande and J. V. Manca, *Appl. Phys. Lett.*, 2009, **95**.
51. F. Padinger, R. S. Rittberger and N. S. Sariciftci, *Adv. Funct. Mater.*, 2003, **13**, 85-88.
52. J. C. Bolsee, W. D. Oosterbaan, L. Lutsen, D. Vanderzande and J. Manca, *Adv. Funct. Mater.*, 2013, **23**, 862-869.
53. E. J. Crossland, K. Tremel, F. Fischer, K. Rahimi, G. Reiter, U. Steiner and S. Ludwigs, *Adv. Mater.*, 2012, **24**, 839-844.
54. M. Pfannmöller, H. Flügge, G. Benner, I. Wacker, C. Sommer, M. Hanselmann, S. Schmale, H. Schmidt, F. A. Hamprecht, T. Rabe, W. Kowalsky and R. R. Schröder, *Nano Lett.*, 2011, **11**, 3099-3107.
55. J. M. Frost, F. Cheynis, S. M. Tuladhar and J. Nelson, *Nano Lett.*, 2006, **6**, 1674-1681.
56. C. Kastner, D. K. Susarova, R. Jadhav, C. Ulbricht, D. A. M. Egbe, S. Rathgeber, P. A. Troshin and H. Hoppe, *J. Mater. Chem.*, 2012, **22**, 15987-15997.
57. P. E. Shaw, A. Ruseckas and I. D. W. Samuel, *Adv. Mater.*, 2008, **20**, 3516-3520.
58. C. M. Rodd and R. Agarwal, *Nano Lett.*, 2011, **11**, 3460-3467.
59. M. J. M. Wirix, P. H. H. Bomans, H. Friedrich, N. A. J. M. Sommerdijk and G. de With, *Nano Lett.*, 2014, **14**, 2033-2038.

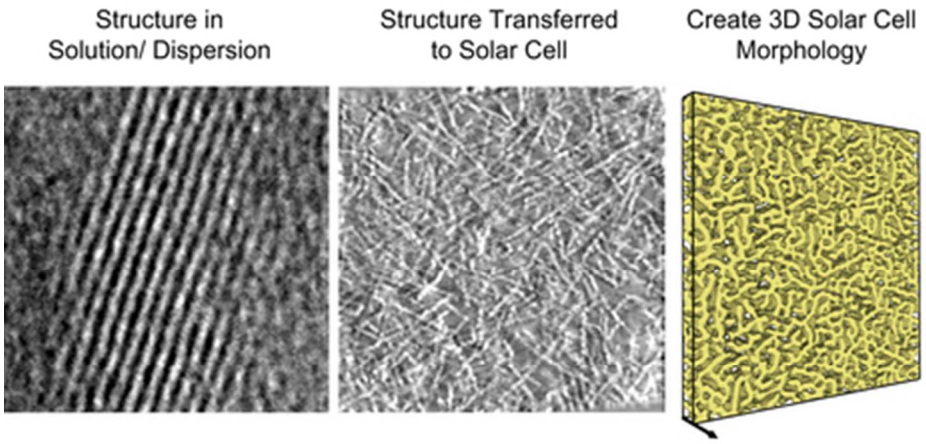

39x19mm (300 x 300 DPI)